Sparse-to-Dense Prediction of Ocean Subsurface Temperature Using Multilevel Spatiotemporal Information Fusion

Lei Lei, *Member, IEEE*, Guidong Yang, *Graduate Student Member, IEEE*, Zuoquan Zhao, Xi Chen, and Ben M. Chen, *Fellow, IEEE*

***Abstract*— Accurately predicting ocean subsurface temperature is vital for advancing ocean and climate research, particularly given the sparse and costly nature of subsurface observations. This study introduces sparse-to-dense prediction of ocean subsurface temperature using multilevel spatiotemporal (ST) information fusion. The framework integrates interpretable ST decoupling, adaptive feature updating, and sparse-to-dense information fusion modules to address the challenge of sparse observations and ever-evolving dynamic environments. Comprehensive experiments focused on the Pacific demonstrate the superiority of the proposed methodology over peer methods. The proposed methodology achieves high-resolution predictions with a root mean square error (RMSE) of 0.2230, an accuracy of 0.9846, and point-wise prediction errors below 0.5 °C under 10% online random sparse observations (ORSOs). Analyses of spatial and temporal temperature dynamics reveal long-term warming trends in the Pacific, including a temperature rise of up to 2.8 °C at −100 m in low-latitude regions over the past 40 years, and identify the latitudinal slope of thermocline dynamics. This study advances the understanding of multiscale thermal processes and variability in the Pacific, demonstrating the potential of application in climate studies, marine resource management, and environmental monitoring.**

***Index Terms*— Global warming, information fusion, Pacific Ocean, remote sensing, subsurface temperature.**

I. Introduction

As THE largest heat sink in the global climate system, the ocean absorbs over 90% of excess atmospheric heat. Recent studies have revealed record-high ocean heat content, with the Pacific Ocean identified as the largest heat reservoir due to its vast surface area [1], [2]. This heat absorption occurs unevenly, both horizontally and vertically, leading to a heterogeneous distribution of water properties. While sea surface temperature dynamics have been extensively studied [3], the ocean subsurface remains less understood due to extreme environmental conditions. Subsurface thermal dynamics are critical for the marine physical, chemical, and biological processes [4].

Ocean dynamics have been studied using numerical modeling and data learning approaches. Traditional numerical models can effectively simulate subsurface ocean dynamics [5], [6], but are often difficult to model accurately due to the gap between actual processes and ideal knowledge [7]. Observations provide foundational and reliable information for data learning approaches. Satellite remote sensing has revolutionized sea surface monitoring [8], while subsurface areas remain poorly observed. The deep ocean remote sensing technologies have shown potential for inferring the internal structure of the ocean from satellite surface observations [9]. However, the uncertain relationship between surface observations and subsurface features limits the accuracy and efficiency. The Argo program, initiated in 2004, has significantly enhanced vertical temperature monitoring, but its spatial coverage remains limited, with sparse observations in tropical and low-latitude areas [10]. Other platforms, such as bathythermographs [11] and survey ships [12], face challenges, including uneven spatial distribution and temporal discontinuities. In the Pacific, the vast and spatiotemporal (ST) heterogeneous nature of the ocean, coupled with strong thermal stratification and dynamic currents, poses significant challenges for subsurface data collection [13]. These observational gaps lead to considerable information loss [14], hindering the ability to accurately study the ST dynamics of the ocean.

Data learning methods show great potential in revealing ocean dynamics due to the improvement of observational data collection and computing power. Statistical approaches [15] have achieved success in simple regression tasks. Machine learning methods, including support vector machines, random forests, and perceptrons [16], [17], offer tools for analyzing straightforward ocean dynamics but often fail to capture the intricate ST dependencies. Recently, deep learning has made significant advancements in ocean modeling [18], [19], with architectures such as convolutional neural networks (CNNs), long short-term memory (LSTM) networks, and Transformers [20], [21], [22]. However, these models face several critical challenges. One major issue is the "non-transparent system" nature of deep learning [23], which limits interpretability and acceptance in remote sensing research. Understanding the

Received 3 January 2025; revised 25 March 2025; accepted 17 April 2025. Date of publication 25 April 2025; date of current version 15 May 2025. This work was supported in part by the Research Grants Council of Hong Kong, SAR, under Grant 14206821, Grant 14217922, Grant 14209623Grant 14209424, and Grant 14200524; in part by the Environment and Conservation Fund of Hong Kong, SAR, under Project 142/2023; and in part by the InnoHK Initiative of the Innovation and Technology Commission of Hong Kong Special Administrative Region Government via Hong Kong Centre for Logistics Robotics. *(Corresponding author: Guidong Yang.)*

The authors are with the Department of Mechanical and Automation Engineering, The Chinese University of Hong Kong, Hong Kong (e-mail: leilei001@cuhk.edu.hk; gdyang@mae.cuhk.edu.hk; zqzhao@mae.cuhk.edu.hk; xichen002@cuhk.edu.hk; bmchen@mae.cuhk.edu.hk).

Digital Object Identifier 10.1109/TGRS.2025.3564468

internal mechanisms driving model predictions is crucial for validating results and ensuring reliability. In addition, these models often struggle to generalize to new and unseen data [24], [25], particularly in dynamic and evolving subsurface environments where real-time processes may differ significantly from the training data. Feature disentanglement (FD) offers a promising solution, demonstrating superior feature interpretability and predictive accuracy [26], [27]. Studies have further shown that stable and dynamic features hidden in systems evolve at different rates, underscoring the need for adaptive approaches to capture these distinct processes effectively [28].

Furthermore, existing deep learning approaches often rely on dense and structured datasets [29], which are scarce in subsurface research due to the high cost and difficulty of acquiring in situ observations. Reconstructing dense spatial fields from limited local sensor information poses a significant challenge. Geometric [30] and interpolation [31], [32] methods have been used to embed unstructured information into CNN architectures to improve prediction accuracy under sparse observation conditions. Cross-attention mechanisms encoded arbitrarily sized sparse input sets into latent spaces, achieving high-precision reconstruction of high-dimensional fields [33], [34]. However, the prediction accuracy of unobserved areas still depends heavily on the distribution density and geometric characteristics of the observation points. Compressed sensing theory has been used to assist the mapping from the original space to the sparse space, improving the robustness of the encoding and decoding processes [35], [36]. This approach emphasizes the crucial role of finding the optimal sparse basis in the decoding or feature extraction process.

Information fusion addresses these challenges by combining data from multiple sources to reduce information loss and enhance accuracy. Previous studies have primarily focused on addressing information loss in remote sensing imagery [37], [38], but little attention has been given to the application of fusion techniques for subsurface temperature. Information fusion can be applied at data, feature, and decision levels, as shown in Fig. 1. Data-level fusion combines raw observations from various sources, such as integrating multispectral sensors with high spectral resolution and narrow spectral bandwidth [39]. However, this approach demands rigorous pre-processing to address ST inconsistencies and observation noise, and missing data. Feature-level fusion integrates extracted complementary features, such as domain-specific descriptors [40], [41]. However, it risks losing subtle information during feature selection, potentially limiting the ability to capture finer patterns. Decision-level fusion combines outputs from multiple local models, providing robustness and scalability for large-scale data scenarios [42]. However, it leads to severe information loss due to its post-processing nature and is most suitable for applications involving massive datasets. A multilevel fusion approach integrates these levels, leveraging their complementary strengths to create a more comprehensive and accurate framework. This holistic strategy is particularly advantageous for reconstructing subsurface ocean temperature fields, which face challenges such as sparse observations, ST heterogeneity, and complex thermal dynamics. By combining data, features, and decisions, multilevel fusion can mitigate information loss, improve spatial and temporal resolution, and enhance predictive accuracy.

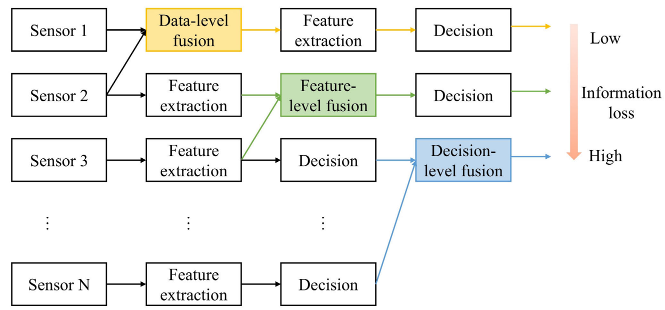

Fig. 1. Information fusion at the data, feature, and decision levels.

Within this context, this article proposes a multilevel ST information fusion framework for sparse-to-dense prediction of subsurface temperature in the Pacific Ocean. The primary innovations of this research are: 1) develop and implement a novel multilevel ST information fusion framework to address sparse observational gaps and enhance prediction resolution; 2) design a hierarchical adaptive feature updating model to capture real-time subsurface thermal structure and changes; and 3) uncover and analyze long-term trends and temperature anomalies in the Pacific Ocean to advance subsurface ocean monitoring. This study aims to improve prediction accuracy under sparse observations while uncovering the deeper mechanisms of Pacific subsurface temperature changes. The proposed framework is expected to produce more accurate and high-resolution subsurface temperature prediction products compared to existing methods.

II. Study Area and Data

The Pacific plays a critical role in regulating global climate variability due to its vast expanse and complex interactions between the atmosphere and ocean. In recent years, Pacific Ocean heat content has reached record levels, with the region projected to remain the most significant heat sink due to its immense area [2]. The Pacific's influence extends to global weather patterns, including El Niñ(o) and La Niña events [43], which drive precipitation anomalies, temperature variability, and shifts in atmospheric circulation. In addition, remote climate systems, such as the Arctic sea ice and the Arctic Oscillation [44], [45], can influence Pacific temperature anomalies through atmospheric teleconnections. These dynamics underscore the need for a detailed understanding and monitoring of the thermal structure, particularly in its subsurface layers, which remain less explored compared to the surface.

The dataset is sourced from the National Marine Data Center of China [46] and provides comprehensive subsurface temperature observations in the Pacific. The original dataset spans a horizontal area from 99°E to 150°E in longitude and from 10°S to 50°N in latitude, with a spatial resolution of 0.5° × 0.5°. Vertically, it includes 35 layers at depths ranging from 7.5 m per layer near the surface to 100 m per layer

TABLE I
DETAILS OF THE PACIFIC OCEAN TEMPERATURE DATASET

Item	Detail
Latitude	0° ~ 30°N
Longitude	140°E ~ 149°E
Depth	-2.5 ~ -1000 m
Historical data range	January 1958 ~ June 1989
Online data range	July 1989 ~ December 2021
Spatial resolution	0.5 °× 0.5°× 1 layer
Temporal resolution	Monthly

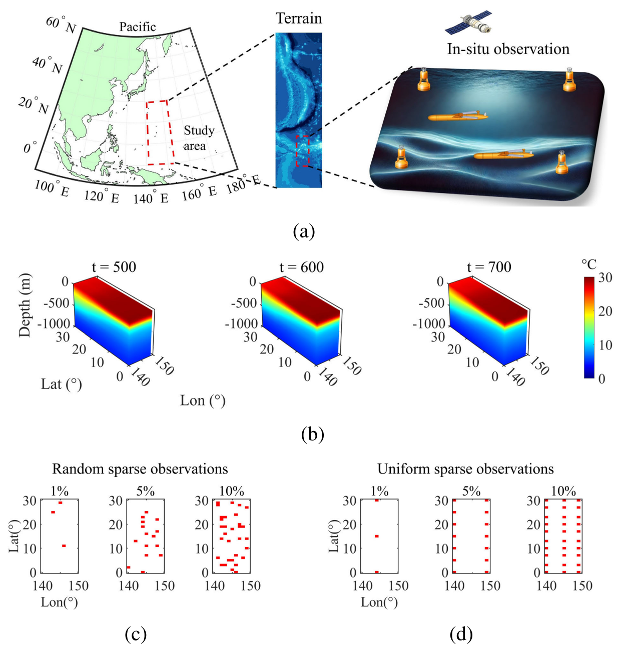

Fig. 2. Pacific Ocean. (a) Study area. (b) Temperature snapshots at t = 500, 600, 700 months. (c) Random sparse observations. (d) Uniform sparse observations.

in deeper regions. The dataset covers a 64-year period with monthly temporal resolution, making it suitable for studying long-term subsurface temperature dynamics. To balance computational efficiency and regional representativeness, this article focuses on a subset, as shown in Fig. 2(a) and detailed in Table I. The selected area spans 140°E–149°E in longitude, 0°N to 30°N in latitude, and depths from −2.5 to −1000 m. This low-latitude to mid-latitude region is particularly suitable for studying subsurface temperature dynamics, given its pronounced thermal gradients, seasonal variability, and relevance to global heat transport. The resulting dataset consists of 24 339 spatial observations per time step across 753 monthly snapshots, offering a robust basis for analysis.

Fig. 2(b) visualizes three representative temperature snapshots, revealing slow 3-D temperature variations over time. Surface temperatures are warmer, decreasing sharply with depth. The thermocline located between −100 and −500 m exhibits the steepest temperature gradient. Below the thermocline, temperature change becomes more uniform, averaging 4 °C–6 °C at −1000 m. ST variability in the thermocline is driven by factors such as sea surface heating, ocean circulation, and climate events. To simulate sparse observational challenges, the study incorporates random and uniform

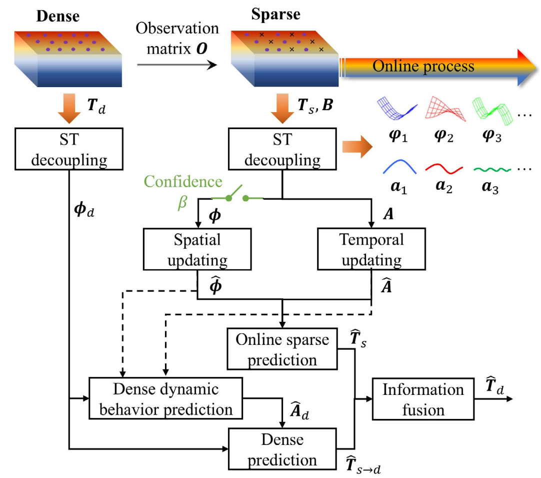

Fig. 3. Framework of the proposed methodology.

sparse distributions ranging from 1% to 10%, as illustrated in Fig. 2(c) and (d). Historical data are treated as dense, providing a rich foundation for analysis, while online observations adopt sparse distributions, reflecting constraints such as limited sensor networks and the high cost of deploying instruments in remote ocean regions.

III. METHODOLOGY DESIGN

A. Framework

Fig. 3 illustrates the proposed methodology, consisting of three key modules designed to address the challenges of sparse observations and ever-evolving dynamic subsurface environments. First, the Pacific temperature data is divided into historical dense data $\boldsymbol{T}_d$ and online sparse observations $\boldsymbol{T}_s$, which are connected by the observation matrix $\boldsymbol{O}$. The high-dimensional temperature field $\boldsymbol{T}_s$ is decoupled by the ST decoupling approach into interpretable stable spatial representations $\boldsymbol{\phi}$ and dynamic temporal behaviors $\boldsymbol{A}$. After that, with real-time observations $\boldsymbol{B}$ arrive, the adaptive feature updating strategy is scheduled by the confidence factor β to update spatial $\hat{\boldsymbol{\phi}}$ and temporal $\hat{\boldsymbol{A}}$ features at different frequencies. Finally, the sparse-to-dense prediction $\hat{\boldsymbol{T}}_d$ integrates the online sparse prediction $\hat{\boldsymbol{T}}_s$ and the dense prediction from the sparse observation $\hat{\boldsymbol{T}}_{s\to d}$. The resolution of the prediction field $\hat{\boldsymbol{T}}_d$ matches that of the original dense observations $\boldsymbol{T}_d$, achieving high-resolution predictions and facilitating a deeper understanding of subsurface dynamic processes.

B. Interpretable ST Decoupling

Accurately modeling ocean dynamics requires reducing the dimensionality of the high-dimensional temperature field while retaining key features. The temperature field $\boldsymbol{T}(\boldsymbol{x}, t) \in \mathbb{R}^{N\times S}$ can be decomposed into stable spatial representations $\boldsymbol{\phi}(\boldsymbol{x})$ and dynamic temporal behaviors $\boldsymbol{A}(t)$

$$\boldsymbol{T}(\boldsymbol{x}, t) = \boldsymbol{\phi}(\boldsymbol{x})\boldsymbol{A}(t) \approx \sum_{i=1}^{r} \boldsymbol{\varphi}_i \boldsymbol{a}_i \tag{1}$$

where r is the model rank, and $\boldsymbol{\varphi_i}$ are sparse and orthogonal basis that satisfy

$$\langle \boldsymbol{\varphi}_i, \boldsymbol{\varphi}_j \rangle = \delta_{ij} \tag{2}$$

where $\langle \cdot, \cdot \rangle$ denotes the inner product and δ_{ij} is the Kronecker delta.

The decoupling solution is derived by solving the eigenvalue problem

$$\int_{\Omega} \boldsymbol{C}(\boldsymbol{x}_j, \boldsymbol{x}_k) \boldsymbol{\varphi}_i(\boldsymbol{x}_k) d\boldsymbol{x} = \lambda_i \boldsymbol{\varphi}_i(\boldsymbol{x}_j) \tag{3}$$

where λ_i and $\boldsymbol{\varphi}_i$ are the eigenvalues and eigenvectors of the temperature field $\boldsymbol{T}$, $\boldsymbol{C}(\boldsymbol{x}_j, \boldsymbol{x}_k)$ is the correlation function of two points j and k, and Ω is the spatial domain.

To capture key spatial and temporal features, an energy criterion is defined as follows:

$$\frac{\sum_{i=0}^{r} \lambda_i}{\sum_{i=0}^{\infty} \lambda_i} \geq \epsilon \tag{4}$$

where $\epsilon \in [0.99, 1]$ is the predefined energy threshold. The r dominant eigenvectors $\boldsymbol{\phi}(\boldsymbol{x}) = [\boldsymbol{\varphi}_1, \ldots, \boldsymbol{\varphi}_r]$ and corresponding $\boldsymbol{A}(t) = [\boldsymbol{a}_1, \ldots, \boldsymbol{a}_r]^{\mathrm{T}}$ can be selected to retain the dominant modes.

C. Adaptive Feature Updating

After ST decoupling of the initial online sparse data $\boldsymbol{T}_s$, an adaptive feature update strategy dynamically adjusts the update interval of spatial and temporal features according to the prediction error. High-frequency dynamic behaviors are updated at regular intervals Δt, while stable representations are updated slowly when the error exceeds a predefined threshold $\mathcal{L}_r$.

The confidence factor β governs the updating of stable representations

$$\beta = \int_0^{\mathcal{L}_r} (p)(\omega) d\omega \tag{5}$$

where $p(\omega)$ is the error density function derived from prediction errors $\mathcal{L}_1$ using a Gaussian kernel $G(\cdot)$

$$p(\omega) = \frac{1}{bt_a} \sum_{k=1}^{t_a} G\left(\frac{\omega - \mathcal{L}_1(k)}{b}\right) \tag{6}$$

where b is the bandwidth, t_a is the update interval for stable representations, and $\mathcal{L}_1$ is the mean square error (mse) between the prediction and truth. Stable representations are updated only when $\mathcal{L}_1 > \mathcal{L}_r$, ensuring model accuracy. If $\mathcal{L}_1 \leq \mathcal{L}_r$, dynamic behaviors are updated to reduce computational overhead while maintaining accuracy.

During this process, real-time data $\boldsymbol{v}_s$ is aligned with the incremental matrix $\boldsymbol{B} \in \mathbb{R}^{N \times t_a}$. After each t_a steps, the matrix is updated, and the initial online sparse data $\boldsymbol{T}_s$ is updated using the bundle matrix

$$\boldsymbol{T}_{s+} \leftarrow \boldsymbol{T}_s + \boldsymbol{B}\boldsymbol{P}^{\mathrm{T}} \tag{7}$$

where $\boldsymbol{P} = \begin{bmatrix} \boldsymbol{0} & \boldsymbol{I} \end{bmatrix}^{\mathrm{T}} \in \mathbb{R}^{S \times t_s}$ integrates new information into the initial data, and $\boldsymbol{I}$ is the identity matrix.

The initial temperature field $\boldsymbol{T}_s$, incremental matrix $\boldsymbol{B}$, and updated temperature field $\boldsymbol{T}_{s+}$ are decoupled via singular value decomposition and QR decomposition [47], respectively

$$\boldsymbol{T}_s = \boldsymbol{\phi}\boldsymbol{\Sigma}\boldsymbol{V}^{\mathrm{T}} \tag{8}$$

$$\boldsymbol{Q}\boldsymbol{R} = (\boldsymbol{I} - \boldsymbol{\phi}\boldsymbol{\phi}^{\mathrm{T}})\boldsymbol{B} \tag{9}$$

$$\begin{aligned} \boldsymbol{T}_{s+} &= \begin{bmatrix} \boldsymbol{\phi}\boldsymbol{\Sigma}\boldsymbol{V}^{\mathrm{T}} & \boldsymbol{B} \end{bmatrix} \\ &= \begin{bmatrix} \boldsymbol{\phi} & \boldsymbol{Q} \end{bmatrix} \begin{bmatrix} \boldsymbol{\Sigma} & \boldsymbol{\phi}^{\mathrm{T}}\boldsymbol{B} \\ \boldsymbol{0} & \boldsymbol{R} \end{bmatrix} \begin{bmatrix} \boldsymbol{V} & \boldsymbol{0} \\ \boldsymbol{0} & \boldsymbol{I} \end{bmatrix}^{\mathrm{T}} \\ &= \hat{\boldsymbol{\phi}}\hat{\boldsymbol{\Sigma}}\hat{\boldsymbol{V}}^{\mathrm{T}} \end{aligned} \tag{10}$$

where $\boldsymbol{Q} \in \mathbb{R}^{N \times q}$ is the orthogonal matrix, $\boldsymbol{R} \in \mathbb{R}^{q \times t_s}$ is the upper triangular matrix, $\begin{bmatrix} \boldsymbol{\Sigma} & \boldsymbol{\phi}^{\mathrm{T}}\boldsymbol{B} \\ \boldsymbol{0} & \boldsymbol{R} \end{bmatrix} = \boldsymbol{\phi}'\boldsymbol{\Sigma}'\boldsymbol{V}'^{\mathrm{T}}$.

The updated stable representations $\hat{\boldsymbol{\phi}}$ combine initial and incremental information

$$\hat{\boldsymbol{\phi}} = [\boldsymbol{\phi}, \boldsymbol{Q}]\boldsymbol{\phi}'. \tag{11}$$

Dynamic behaviors capture nonlinear, rapid changes and are computed as follows:

$$\boldsymbol{A}(t) = \hat{\boldsymbol{\phi}}^{\mathrm{T}}\boldsymbol{T}_{s+}. \tag{12}$$

Dynamic behaviors are modeled using a retrospective batch process, where the current signal $\boldsymbol{A}(t)$ depends on p time-lagged states. The neural network is used to capture nonlinear temporal dependencies, with the prediction given by the following equation:

$$\hat{\boldsymbol{A}}(t) = \boldsymbol{W}_{t-1}^{\mathrm{T}}\boldsymbol{h}_{t-1}(\boldsymbol{A}(t - \Delta t), \ldots, \boldsymbol{A}(t - p\Delta t)) \tag{13}$$

where $\boldsymbol{W}$ is the weight matrix, updated by Lyapunov-based weight rule [48], and $\boldsymbol{h}$ is the activation function.

D. Sparse-to-Dense Information Fusion

The framework combines historical dense data with online sparse observations to solve the problem of information loss caused by sparse observations. The spatial observation matrix $\boldsymbol{O}$ is used to project the historical dense data $\boldsymbol{T}_d$ onto the sparse observation grid

$$\boldsymbol{T}_{d \to s} = \boldsymbol{O}\boldsymbol{T}_d \tag{14}$$

where $\boldsymbol{T}_{d \to s}$ is the historical dense data restricted to the sparse observation grid.

The online sparse prediction and historical dense data are separated to obtain stable spatial representations and dynamic temporal behaviors

$$\hat{\boldsymbol{T}}_s = \hat{\boldsymbol{\phi}}\hat{\boldsymbol{A}} \tag{15}$$

$$\boldsymbol{T}_d = \boldsymbol{\phi}_d\boldsymbol{A}_d. \tag{16}$$

The online sparse prediction is expended to the dense field

$$\hat{\boldsymbol{T}}_{s \to d} = \boldsymbol{\phi}_d\hat{\boldsymbol{A}}_d \tag{17}$$

where $\hat{\boldsymbol{T}}_{s \to d}$ is the dense prediction from the sparse observations, and $\hat{\boldsymbol{A}}_d$ is the dense dynamic behavior derived from the online sparse dynamic behavior via the pseudo-inverse operation $(\cdot)^{\dagger}$

$$\hat{\boldsymbol{A}}_d = \left(\hat{\boldsymbol{\phi}}^{\mathrm{T}}\boldsymbol{O}\boldsymbol{\phi}_d\right)^{\dagger}\hat{\boldsymbol{A}}. \tag{18}$$

By combining the online predictions from the sparse observation with the dense expanded predictions from the pseudo-inverse operation, the sparse-to-dense predictions can be reconstructed

$$\hat{\boldsymbol{T}}_d = \begin{cases} \hat{\boldsymbol{T}}_s = \hat{\boldsymbol{\phi}}\hat{\boldsymbol{A}}, & \text{observed} \\ \hat{\boldsymbol{T}}_{s\to d} = \boldsymbol{\phi}_d\left(\hat{\boldsymbol{\phi}}^{\mathrm{T}}\boldsymbol{O}\boldsymbol{\phi}_d\right)^{\dagger}\hat{\boldsymbol{A}}, & \text{otherwise.} \end{cases} \tag{19}$$

E. Model Implementation

The implementation process of the proposed methodology is detailed in Algorithm 1, which outlines the workflow for sparse-to-dense prediction of ocean subsurface temperature using multilevel ST information fusion. The process begins with ST decoupling, extracting stable spatial representations and dynamic temporal behaviors from historical dense data and initial online sparse observations. Stable representations capture persistent spatial features, while dynamic behaviors model temporal uncertainties in the data. To ensure adaptability, adaptive feature updating is incorporated to dynamically refine stable representations and update dynamic behaviors to adjust to evolving subsurface conditions efficiently. The adaptive feature updating strategy ensures computational efficiency by selectively updating features based on prediction error thresholds. Finally, the ST information fusion is utilized to reconstruct and forecast the dense subsurface temperature field, combining the strengths of sparse observations and historical dense data.

Algorithm 1 Sparse-to-Dense Prediction of Ocean Subsurface Temperature Using Multilevel ST Information Fusion

Require: Historical dense data $\boldsymbol{T}_d$, initial online sparse observations $\boldsymbol{T}_s$
Ensure: Sparse-to-dense prediction $\hat{\boldsymbol{T}}_d$

```
Initialization:
Extract φ_d and A_d from T_d using Eq. (16)
Extract φ and A from T_s using Eq. (1)
Randomly initialize LSTM weights
Set time step t ← 0
while Real-time monitoring is active do
   Obtain real-time sparse data v_s
   Append v_s to the incremental matrix B
   Update online sparse observations T_{s+} using Eq. (7)
   Calculate prediction error L_1 and threshold L_r using Eq. (5)
   if L_1 > L_r then
      Fine-tune stable representations φ̂ using Eq. (11)
   else
      Compute dynamic behaviors A using Eq. (12)
      Update LSTM weights
      Predict future dynamic behaviors Â using Eq. (13)
   end if
   Compute dense dynamic behaviors Â_d using Eq. (18)
   Fuse φ̂ and Â for T̂_s using Eq. (15)
   Fuse φ_d and Â_d for T̂_{s→d} using Eq. (17)
   Perform information fusion T̂_d using Eq. (19)
   Advance time t ← t + Δt
end while
```

IV. Experimental Studies

A. Experimental Setting

The energy threshold is set to $\epsilon = 0.99$, and the confidence factor for feature updating is set to $\beta = 0.95$. The input has a dimension of $[r, 12]$, where r denotes the model rank ($r = 15$ and 16 for $\hat{\boldsymbol{A}}_d$ and $\hat{\boldsymbol{A}}$, respectively), and 12 represents the number of past time steps used for prediction. The historical dense data consists of the first 50% of the dataset, while the last 50% is configured with sparse observations distributed either uniformly or randomly.

The proposed methods are compared with five peer methods used in environment prediction. For the comparison under original dense observations, Conv-LSTM [20] integrates CNN with LSTM, making it well suited for modeling spatial and temporal dependencies in sequence data. 3D-CNN [21] extends CNN to three dimensions, enabling modeling of spatial relationships in 3-D data, thereby enhancing its ability to capture complex patterns of ocean temperature distribution over time. In addition, FD [27] uses Tucker decomposition for feature extraction and a probabilistic incremental learning method to update the temporal signal. For the comparison under sparse observations, Voronoi tessellation [30] combined with CNN can significantly improve the prediction accuracy under sparse conditions. Senseiver [33] uses an encoder–decoder structure with a cross-attention mechanism to achieve high-precision reconstruction of sparse observations.

To evaluate the performance of the proposed methodology and benchmark models, seven widely adopted evaluation metrics are used: root mse (RMSE), mean absolute error (MAE), accuracy (ACC), coefficient of determination (R^2), average error (Avg error), percent bias, and point-wise prediction error distribution

$$\mathrm{RMSE} = \sqrt{\frac{1}{n}\sum_{i=1}^{n}\left(y_i - \hat{y}_i\right)^2} \tag{20}$$

$$\mathrm{MAE} = \frac{1}{n}\sum_{i=1}^{n}\left|y_i - \hat{y}_i\right| \tag{21}$$

$$\mathrm{ACC} = 1 - \frac{1}{n}\sum_{i=1}^{n}\left(\frac{\left|y_i - \hat{y}_i\right|}{y_i}\right) \tag{22}$$

$$R^2 = 1 - \frac{\sum_{i=1}^{n}\left(y_i - \hat{y}_i\right)^2}{\sum_{i=1}^{n}\left(y_i - \bar{y}\right)^2} \tag{23}$$

$$\text{Avg error} = \frac{1}{n}\sum_{i=1}^{n}\left(y_i - \hat{y}_i\right) \tag{24}$$

$$\text{Percent bias} = \frac{\sum_{i=1}^{n}\left(y_i - \hat{y}_i\right)}{\sum_{i=1}^{n} y_i} \times 100 \tag{25}$$

where y_i and $\hat{y}_i$ are the observed and predicted values, $\bar{y}$ is the mean, and n is the number of samples.

B. Spatial and Temporal Features

Fig. 4 visualizes the decoupled spatial and temporal features under 10% online random sparse observation (ORSO), highlighting the first three features. The ST decoupling method

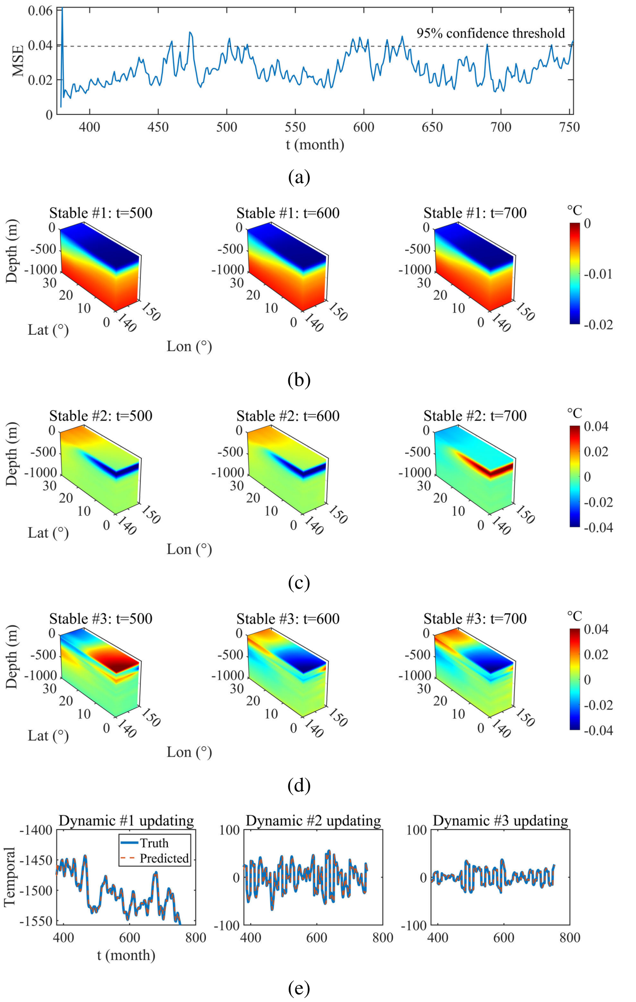

Fig. 4. Spatial and temporal features under 10% ORSO. (a) Adaptive feature updating based on confidence evaluation, (b) stable #1, (c) stable #2, (d) stable #3, and (e) dynamic #1–#3.

effectively separates the observation into interpretable stable representations and dynamic behaviors. Fig. 4(a) illustrates the adaptive feature updating process triggered by confidence evaluation. Specifically, when the mse exceeds the 95% confidence threshold, a stable spatial feature update is triggered to enhance the accuracy of model predictions. The dynamic temporal features are updated continuously at regular intervals to maintain predictive reliability. Stable #1 in Fig. 4(b) captures persistent and large-scale spatial features, such as temperature gradients that vary with depth, reflecting stable ocean structure. Subsequent stable #2 and #3 in Fig. 4(c) and (d) reveal more subtle phenomena, such as thermoclines and boundary effects, highlighting local variations. The slow updates to these features, especially the nearly constant nature of stable #1, emphasize the robustness and reliability of the decoupled process in representing stable environmental structures. Dynamic #1 in Fig. 4(e) shows that the dominant modes have higher amplitudes and contribute significantly to the system dynamics. Minor modes reflect local or transient effects and require more frequent updates to track real-time changes.

Table II evaluates the contribution of each module in the proposed methodology under 10% ORSO. First,

TABLE II

Ablation Experiments Under 10% ORSO

Decoupling	Updating	Fusion	RMSE	MAE	ACC	R^2
✓	×	×	22.9985	21.6868	N/A	N/A
✓	✓	×	0.5492	0.4937	0.9667	0.9962
✓	✓	✓	0.2230	0.2055	0.9834	0.9994

TABLE III

Sparse-to-Dense Prediction Performance Under Different Sparsity Levels

Distribution	Sparsity (%)	RMSE	MAE	ACC	R^2
Dense	100	0.1321	0.0914	0.9879	0.9998
Uniform	1	0.2536	0.2276	0.9827	0.9992
	5	0.2522	0.2285	0.9833	0.9992
	10	0.2473	0.2251	0.9834	0.9992
Random	1	0.2434	0.2211	0.9845	0.9993
	5	0.2245	0.2072	0.9845	0.9994
	10	0.2230	0.2055	0.9846	0.9994

ST decoupling alone is not sufficient to capture the system dynamics, resulting in not applicable (N/A). Adaptive feature updating is crucial to capture the evolution of the system, achieving an RMSE of 0.5492. The sparse-to-dense information fusion module is essential to address the challenges of information loss, missing data, and environmental uncertainties. This module enables the model to accurately infer unobserved data points by combining historical data with online observations. When sparse-to-dense information fusion is activated, the model performs best, with the RMSE further reduced to 0.2230. Each module plays a unique and complementary role in accurately modeling and predicting subsurface dynamics, even under sparse observations.

C. Sparse-to-Dense Prediction

Table III summarizes the sparse-to-dense prediction results under different sparsity levels and distributions. The results demonstrate a clear improvement in prediction accuracy as the sparsity level decreases and more observation points. For example, under a uniform sparsity of 1%, the model achieves an RMSE of 0.2536, an MAE of 0.2276, an ACC of 0.9827, and an R^2 score of 0.9992. When the uniform sparsity increases to 10%, the prediction performance improves significantly, with the RMSE dropping to 0.2473 and the ACC reaching 0.9834, demonstrating the benefits of having more observation points to enhance spatial coverage. The prediction performance under online dense observations wins the best, with an RMSE of 0.1321 and an ACC of 0.9879. In addition, at the same sparsity level, the random distribution consistently outperforms the uniform distribution. Under a random sparsity of 10%, the model achieves an RMSE of 0.2230 and an ACC of 0.9846. The random distribution provides a more diverse and representative sampling than the uniform distribution.

Fig. 5 presents the sparse-to-dense prediction fitting performance under different random sparsity levels. The results show that the high-temperature regions near the surface and the low-temperature regions at deeper depths are relatively

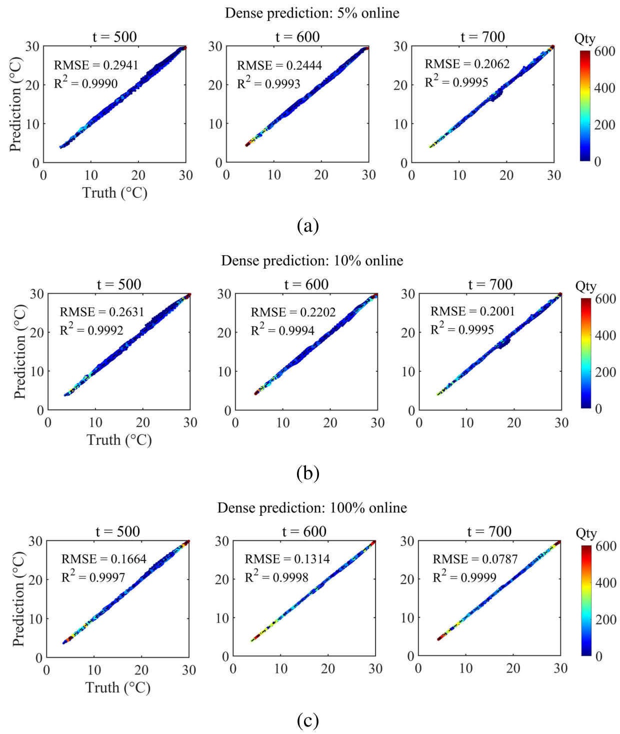

Fig. 5. Sparse-to-dense prediction fitting at $t = 500$, 600, 700 months. (a) Dense prediction under 5% ORSO. (b) Dense prediction under 10% ORSO. (c) Dense prediction under online dense observations.

well represented because they are more uniform and stable. However, the thermocline with higher variability and steeper temperature gradients is more sensitive to observation sparsity, and incorporating more observations provides better spatial representation and prediction reliability. For example, under 5% and 10% ORSO in Fig. 5(a) and (b), the dense prediction shows noticeable deviations in thermocline regions with complex thermal gradients. Under online dense observations in Fig. 5(c), the model achieves the highest accuracy and captures detailed thermal structures with negligible errors. In addition, the adaptive feature updating strategy continuously integrates new observations, enabling the model to adapt and improve its predictions over time.

Fig. 6 further demonstrates the significant impact of resolution on the quality and accuracy of temperature predictions. In Fig. 6(a), under 1% ORSO, the same resolution of sparse prediction exhibits severe information loss and distortion, with minimal spatial variation and failure to capture fine structures such as local anomalies or detailed gradients. As the number of observation points increases in Fig. 6(b) and (c), the sparse prediction shows clear spatial trends, such as temperature gradients. However, the sparse prediction still lacks finer details, with local anomalies and precise temperature transitions difficult to resolve. In contrast, the proposed sparse-to-dense prediction in Fig. 6(d) provides a detailed and accurate representation of the temperature field. It effectively captures the horizontal variation and temperature gradients along the latitude line, ranging from 30 °C to 26 °C. This high-resolution forecast reveals subtle features such as sharp gradients, local thermal anomalies, and the complex interplay of environmental factors that shape the subsurface thermal structure.

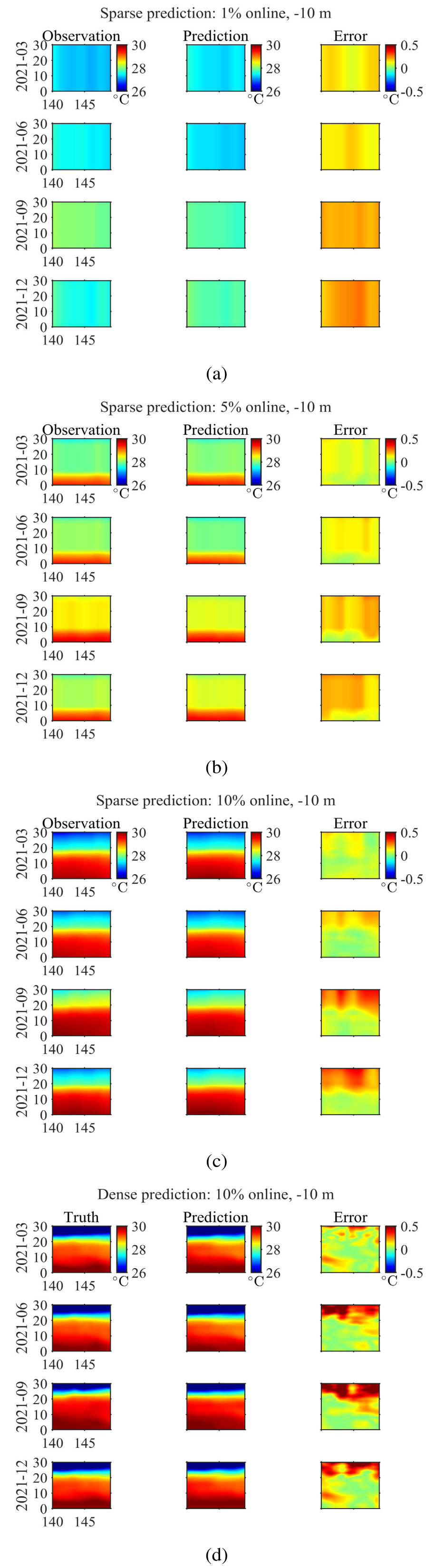

Fig. 6. Prediction resolution comparison at a depth of −10 m. (a) Sparse prediction under 1% ORSO. (b) Sparse prediction under 5% ORSO. (c) Sparse prediction under 10% ORSO. (d) Dense prediction under 10% ORSO.

TABLE IV
COMPARISON WITH DIFFERENT PREDICTION METHODS

Distribution	Method	RMSE	MAE	ACC	R^2
Dense	Conv-LSTM [20]	0.6898	0.3024	0.9535	0.9943
	3D-CNN [21]	0.5174	0.2568	0.9832	0.9955
	FD [27]	0.3991	0.1322	0.9857	0.9968
	Proposed	0.1321	0.0914	0.9879	0.9998
10% ORSO	Voronoi [30]	0.4992	0.5316	0.9411	0.9916
	Senseiver [33]	0.2679	0.2150	0.9840	0.9991
	Proposed	0.2230	0.2055	0.9846	0.9994

The comparative results in Table IV demonstrate the superior performance of the proposed methodology across all evaluation metrics. Under dense observations, Conv-LSTM [20] and 3D-CNN [21] lack support for incremental updates, limiting their applicability in dynamic environments. FD [27] incorporates Tucker decomposition and incremental learning and demonstrates improved adaptability and performance, with an RMSE of 0.3991 and an ACC of 0.9857. These methods for dense observations are difficult to directly apply to learning with sparse observation data. Under 10% ORSO, Voronoi [30] and Senseiver [33] show some effectiveness in handling sparse observations and generating dense predictions. However, both methods primarily focus on spatial modeling while neglecting temporal dependencies and system evolution, which significantly hinders their ability to adapt to dynamic environments. In summary, the proposed methodology effectively integrates interpretable ST modeling, adaptive feature updating, and multilevel information fusion, with an RMSE of 0.1321 and an ACC of 0.9879 under dense observations and an RMSE of 0.2230 and an ACC of 0.9946 under 10% ORSO, demonstrating its robustness and scalability across diverse scenarios.

D. Spatial and Temporal Dynamics

Fig. 7 illustrates the seasonal variation of subsurface temperatures at different depths, showcasing the intricate ST dynamics of the subsurface thermal structure. The predictions align closely with the truth, with most errors remaining within 0.5 °C. In the upper layers shown in Fig. 7(a) and (b), seasonal fluctuations are more pronounced, primarily driven by changes in solar radiation, wind stress, and atmospheric conditions, resulting in significant temperature variability and a highly dynamic thermal structure. At greater depths in Fig. 7(c) and (d), temperature variations diminish, and stability increases. Below −500 m, the thermal structure remains relatively consistent throughout the year, highlighting the insulating effect of ocean depth. Spatially, upper-layer temperatures are highest at low latitudes, where solar heating is most intense. However, deeper layers exhibit a temperature peak at mid-latitudes, likely influenced by ocean currents and the gradual progression of temperature gradients. This latitudinal difference and vertical temperature dynamics create a complex thermal structure shaped by the interplay of multiple physical processes, including circulation patterns, stratification, and heat transport. Despite these complexities, the proposed methodology accurately predicts subsurface temperatures.

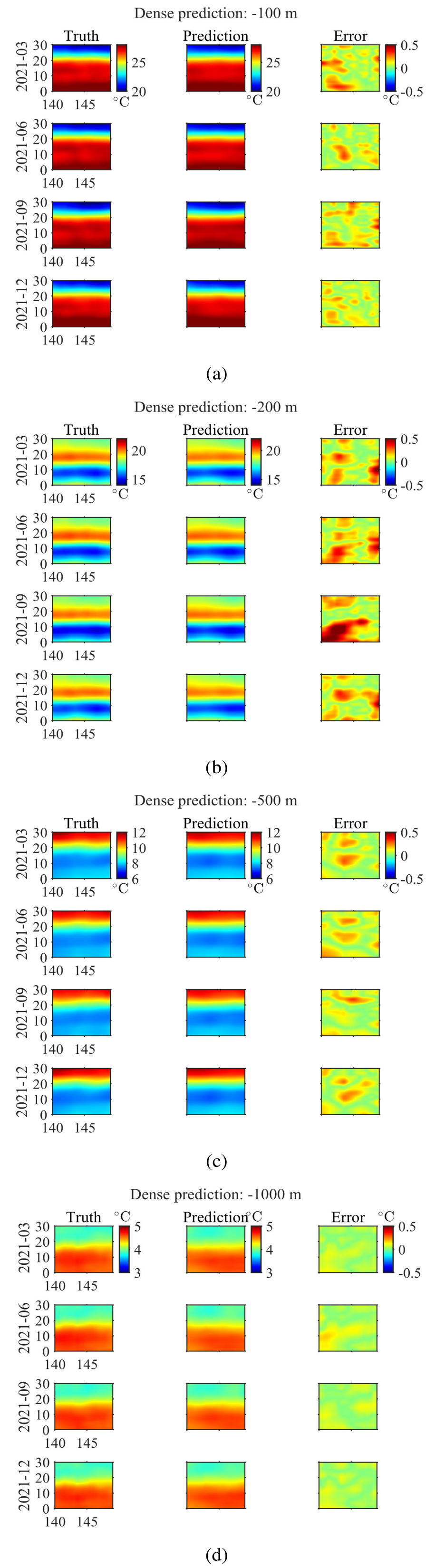

Fig. 7. Temperature seasonal variation in 2021 across different depths under 10% ORSO. (a) Depth −100 m. (b) Depth −200 m. (c) Depth −500 m. (d) Depth −1000 m.

Fig. 8 illustrates the long-term variation of subsurface temperatures across different depths, revealing significant spatial

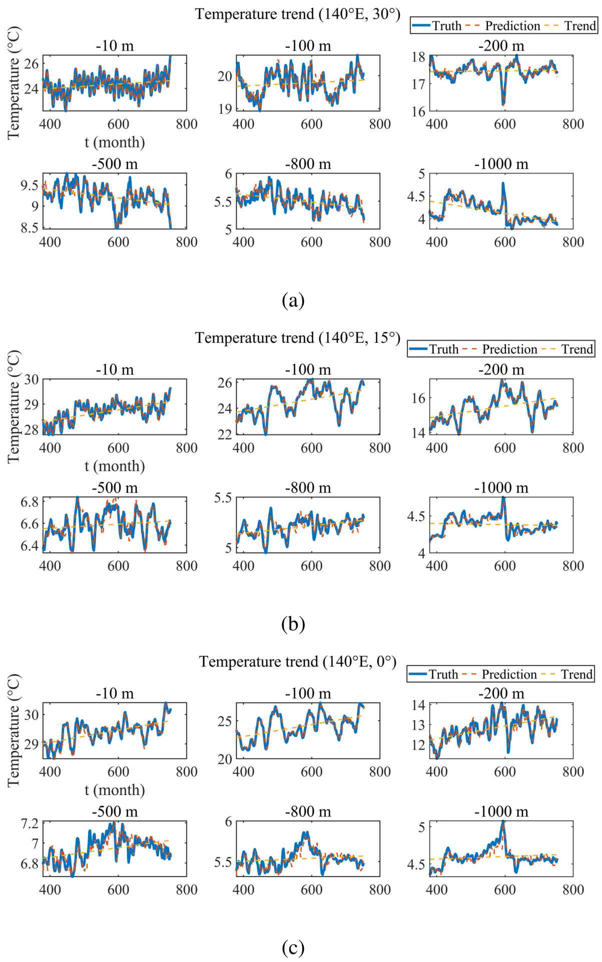

Fig. 8. Long-term variation of subsurface temperatures under 10% ORSO (July 1989 to December 2021). (a) Location (140°E, 30°N). (b) Location (140°E, 15°N). (c) Location (140°E, 0°).

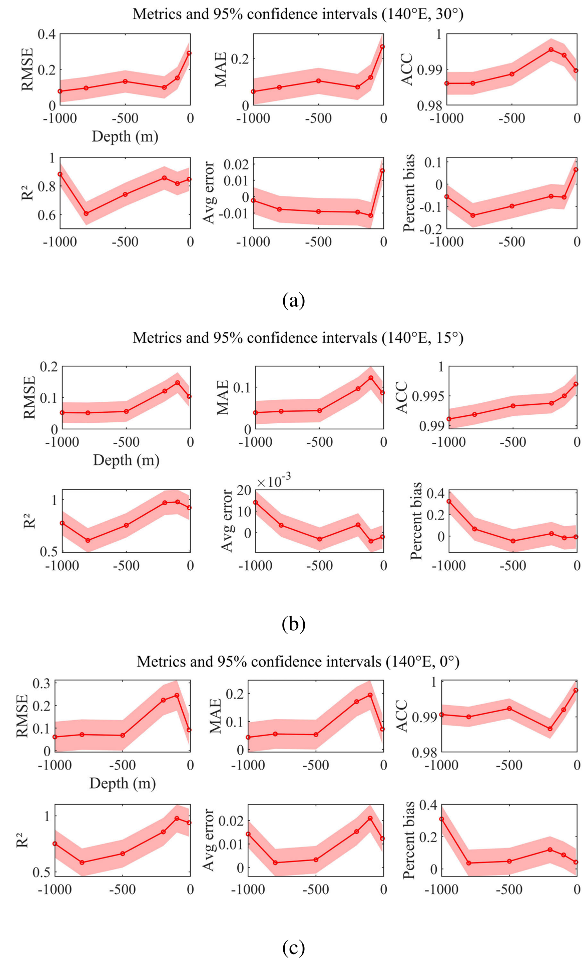

Fig. 9. Prediction performance under 10% ORSO (July 1989 to December 2021). (a) Location (140°E, 30°N). (b) Location (140°E, 15°N). (c) Location (140°E, 0°).

and temporal heterogeneity in ocean warming trends. For example, at mid-latitude regions in Fig. 8(a), water warming is less pronounced, reflecting the moderating influence of atmospheric variability, wind-driven mixing, and ocean currents in subtropical regions. These factors distribute heat more evenly, reducing localized temperature increases. However, at low-latitude -100 m in Fig. 8(c), long-term monitoring indicates a temperature rise of approximately 2.8 °C over the past 40 years. Such trends align with broader global patterns of ocean warming, emphasizing the role of the Pacific Ocean subsurface in storing heat and buffering atmospheric temperature changes. Overall, the observed differences between low-latitude and mid-latitude regions underscore the spatial heterogeneity in the ocean's thermal response. Low-latitude regions, being closer to the equator, experience intense solar radiation and stronger stratification, which amplify surface warming and limit heat penetration to deeper layers. Mid-latitude regions, influenced by more variable atmospheric conditions and stronger ocean currents, exhibit a more balanced thermal response, with less surface warming and localized cooling at greater depths.

Moreover, Fig. 9 illustrates the prediction performance across different depths (with 95% confidence intervals). The results show that the model maintains consistent accuracy, as indicated by the limited range of prediction errors and tight confidence intervals at different latitudes and depths. Prediction performance increases toward stable deep layers and decreases at thermoclines with transient features. For example, at all locations, metrics such as RMSE and MAE increase toward the upper layers between 0 and -500 m and decrease toward the deep layers. Average error and percent bias further highlight the modeling accuracy. The percent bias reveals regional differences, with low-latitude regions showing higher biases, reflecting challenges in capturing thermal fluctuations.

E. Temperature Anomaly Analysis

Fig. 10 presents the Pacific OTA over the past 40 years, calculated relative to the mean temperature at each spatial point over time. The close alignment between the truth in Fig. 10(a) and predicted OTA in Fig. 10(b) highlights the modeling accuracy and robustness for capturing complex subsurface temperature dynamics. Mid-latitude regions (140°E, 30°N) exhibit fewer anomalies. This stability can be attributed to the moderating effects of stronger wind-driven mixing and ocean currents, which help distribute heat more evenly and dampen localized fluctuations. Significant periodic OTA is

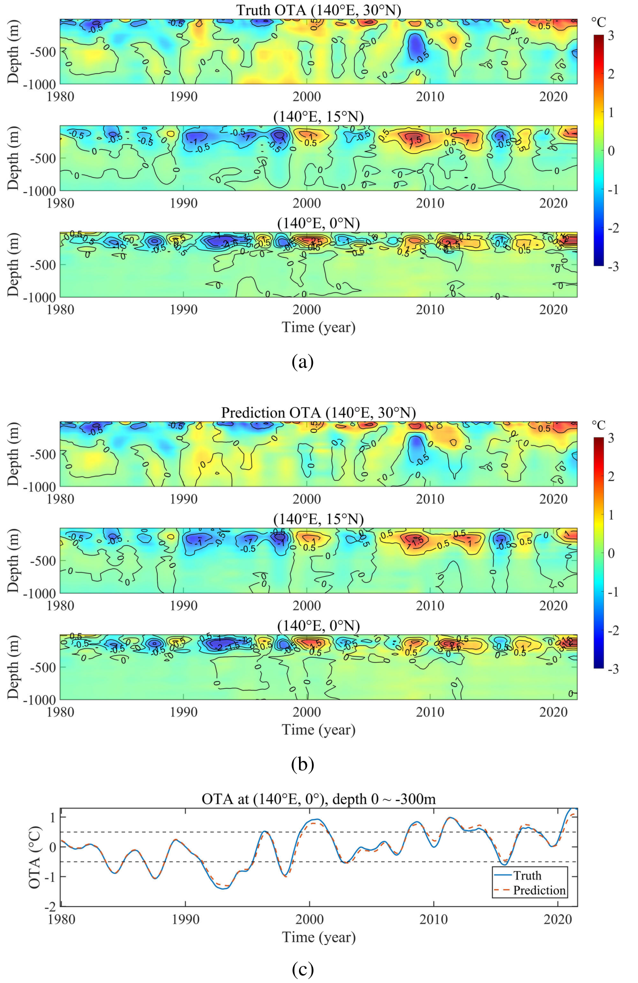

Fig. 10. Pacific OTA analysis over the past 40 years. (a) Truth. (b) Prediction under 10% ORSO. (c) Pacific subsurface temperature oscillations analysis.

observed in the upper layers between 0 and −300 m, with the most pronounced anomalies occurring in low-latitude regions (140°E, 0°) and (140°E, 15°N). These anomalies are primarily driven by intensified solar heating, reduced vertical mixing, and the overarching effects of global warming, which amplify temperature variability in the upper ocean. Interannual oscillations of subsurface temperatures, particularly those linked to El Niñ(o)-Southern Oscillation (ENSO) events, further contribute to the observed peaks and fluctuations, reflecting the dynamic interplay between atmospheric and oceanic processes. Fig. 10(c) displays the OTA time series averaged over the upper 0 to −300 m at (140°E, 0°) from 1980 to 2023. The model accurately captures both the positive OTA peaks and the negative OTA troughs. There are partial discrepancies between the OTA peaks/troughs in Fig. 10(c) and the canonical ENSO signal in the traditional monitoring region, due to the geographic separation and distinct ocean-atmosphere dynamics [49]. At greater depths beyond −300 m, temperature distributions remain relatively stable across all regions, with no significant anomalies. This stability underscores the insulating effects of vertical stratification, which inhibits the rapid propagation of surface heat into deeper layers.

V. Conclusion

In this study, we propose a novel multilevel ST information fusion framework for sparse-to-dense prediction of subsurface temperature, with a focus on the Pacific Ocean. The framework effectively decouples high-dimensional subsurface temperature fields into interpretable low-dimensional spatial and temporal features. Using a confidence-driven scheduling mechanism, stable spatial representations are updated incrementally to capture gradual changes, while dynamic temporal behaviors are updated more frequently to reflect fast-varying uncertainties. In addition, the incorporation of the sparse-to-dense information fusion module compensates for the limitations of online sparse observations, significantly improving predictive accuracy, resolution, and robustness.

Comprehensive experiments demonstrate the superiority of the proposed methodology over peer methods. The proposed methodology consistently achieves high performance across varying sparsity levels and spatial distributions, with an RMSE of 0.2230 and an ACC of 0.9846 under 10% ORSO. The model successfully captures long-term warming trends in the Pacific and depth-dependent dynamics, including the latitudinal slope of the thermocline and localized cooling at −1000 m in mid-latitudes. Moreover, the Pacific OTA analysis revealed drastic temperature changes in low-latitude regions and significant mid-latitude warming. These findings highlight the ST heterogeneity of ocean subsurface temperature and the dynamic interplay between atmospheric and oceanic processes. In summary, the proposed methodology exhibits excellent ability to reconstruct and analyze subsurface temperature fields even under sparse observations. It holds significant potential for advancing remote sensing applications in climate studies, marine resource management, and oceanographic research.

In the future, the framework can be extended to predict other important ocean parameters with similar ST dynamics. Moreover, analyzing global subsurface temperature anomalies and inter-basin interactions will further advance the interpretability of ocean ST dynamics.

Acknowledgment

The data support from the National Marine Data Center of China (http://mds.nmdis.org.cn).

References

[1] D. Obura et al., "Vulnerability to collapse of coral reef ecosystems in the Western Indian ocean," *Nature Sustainability*, vol. 5, no. 2, pp. 104–113, Dec. 2021.

[2] L. Cheng et al., "Past and future ocean warming," *Nature Rev. Earth Environ.*, vol. 3, no. 11, pp. 776–794, Oct. 2022.

[3] B. H. Samset, M. T. Lund, J. S. Fuglestvedt, and L. J. Wilcox, "2023 temperatures reflect steady global warming and internal sea surface temperature variability," *Commun. Earth Environ.*, vol. 5, no. 1, p. 460, Aug. 2024.

[4] S. S. U. H. Kazmi, Y. Y. L. Wang, Y.-E. Cai, and Z. Wang, "Temperature effects in single or combined with chemicals to the aquatic organisms: An overview of thermo-chemical stress," *Ecolog. Indicators*, vol. 143, Oct. 2022, Art. no. 109354.

[5] S. Koga and M. Krstic, "Arctic sea ice state estimation from thermodynamic PDE model," *Automatica*, vol. 112, Feb. 2020, Art. no. 108713.

[6] R. M. Holmes, J. D. Zika, S. M. Griffies, A. M. Hogg, A. E. Kiss, and M. H. England, "The geography of numerical mixing in a suite of global ocean models," *J. Adv. Model. Earth Syst.*, vol. 13, no. 7, Jul. 2021, Art. no. e2020MS002333.

[7] P. Tahmasebi, S. Kamrava, T. Bai, and M. Sahimi, "Machine learning in geo- and environmental sciences: From small to large scale," *Adv. Water Resour.*, vol. 142, Aug. 2020, Art. no. 103619.

[8] C. Shi, X. Zheng, Z. Zhao, K. Zhang, Z. Su, and Q. Lu, "LSKF-YOLO: Large selective kernel feature fusion network for power tower detection in high-resolution satellite remote sensing images," *IEEE Trans. Geosci. Remote Sens.*, vol. 62, 2024, Art. no. 5620116.

[9] H. Su, J. Qiu, Z. Tang, Z. Huang, and X.-H. Yan, "Retrieving global ocean subsurface density by combining remote sensing observations and multiscale mixed residual transformer," *IEEE Trans. Geosci. Remote Sens.*, vol. 62, 2024, Art. no. 4201513.

[10] D. Roemmicha et al., "The Argo program," in *Partnerships in Marine Research: Case Studies, Lessons Learned, and Policy Implications*. San Diego, CA, USA: Elsevier, 2021, p. 53.

[11] S. Simoncelli, F. Reseghetti, C. Fratianni, L. Cheng, and G. Raiteri, "Reprocessing of eXpendable BathyThermograph (XBT) profiles from the ligurian and tyrrhenian seas over the time period 1999–2019 with a full metadata upgrade," *Earth Syst. Sci. Data*, vol. 16, no. 12, pp. 5531–5561, Dec. 2024.

[12] S. Aslam, M. P. Michaelides, and H. Herodotou, "Internet of ships: A survey on architectures, emerging applications, and challenges," *IEEE Internet Things J.*, vol. 7, no. 10, pp. 9714–9727, Oct. 2020.

[13] G. C. Johnson et al., "Argo—Two decades: Global oceanography, revolutionized," *Annu. Rev. Mar. Sci.*, vol. 14, no. 1, pp. 379–403, Jan. 2022.

[14] Y. Wang, X. Zhan, J. Gao, J. Yao, S. Wei, and J. Bai, "Array SAR 3-D sparse imaging based on regularization by denoising under few observed data," *IEEE Trans. Geosci. Remote Sens.*, vol. 62, 2024, Art. no. 5213114.

[15] Z. Zuo, J. Nie, Q. Wen, M. Ye, Y. Diao, and X. Chen, "DINFNN: Data inpainting Fourier neural network for cloud-induced extensive missing area in sea surface temperature," *IEEE Trans. Geosci. Remote Sens.*, vol. 62, 2024, Art. no. 4212414.

[16] Q. Zhao, Y. Liu, W. Yao, and Y. Yao, "Hourly rainfall forecast model using supervised learning algorithm," *IEEE Trans. Geosci. Remote Sens.*, vol. 60, 2022, Art. no. 4100509.

[17] D. Degen et al., "Perspectives of physics-based machine learning strategies for geoscientific applications governed by partial differential equations," *Geosci. Model Develop.*, vol. 16, no. 24, pp. 7375–7409, Dec. 2023.

[18] S. Thiria et al., "Downscaling of ocean fields by fusion of heterogeneous observations using deep learning algorithms," *Ocean Model.*, vol. 182, Apr. 2023, Art. no. 102174.

[19] C. Xiao et al., "Prediction of long lead monthly three-dimensional ocean temperature using time series gridded Argo data and a deep learning method," *Int. J. Appl. Earth Observ. Geoinf.*, vol. 112, Aug. 2022, Art. no. 102971.

[20] K. Zhang, X. Geng, and X.-H. Yan, "Prediction of 3-D ocean temperature by multilayer convolutional LSTM," *IEEE Geosci. Remote Sens. Lett.*, vol. 17, no. 8, pp. 1303–1307, Aug. 2020.

[21] B. Qiao, Z. Wu, Z. Tang, and G. Wu, "Sea surface temperature prediction approach based on 3D CNN and LSTM with attention mechanism," in *Proc. 23rd Int. Conf. Adv. Commun. Technol. (ICACT)*, Feb. 2021, pp. 342–347.

[22] S. Zhang et al., "Spatial–temporal Siamese convolutional neural network for subsurface temperature reconstruction," *IEEE Trans. Geosci. Remote Sens.*, vol. 62, 2024, Art. no. 4501416.

[23] Y. Liu, K. Duffy, J. G. Dy, and A. R. Ganguly, "Explainable deep learning for insights in el Niño and river flows," *Nature Commun.*, vol. 14, no. 1, p. 339, Jan. 2023.

[24] L. Ren, T. Mo, and X. Cheng, "Meta-learning based domain generalization framework for fault diagnosis with gradient aligning and semantic matching," *IEEE Trans. Ind. Informat.*, vol. 20, no. 1, pp. 1–11, Jan. 2024.

[25] T. Kapoor, A. Chandra, D. M. Tartakovsky, H. Wang, A. Núñez, and R. Dollevoet, "Neural oscillators for generalization of physics-informed machine learning," in *Proc. AAAI Conf. Artif. Intell.*, Jan. 2023, pp. 13059–13067.

[26] Q. Guo, H. Xu, and F. Xu, "Causal adversarial autoencoder for disentangled SAR image representation and few-shot target recognition," *IEEE Trans. Geosci. Remote Sens.*, vol. 61, 2023, Art. no. 5221114.

[27] L. Lei and Z. Jianxing, "Feature disentanglement learning model for ocean temperature field forecast," *Appl. Math. Model.*, vol. 117, pp. 549–562, May 2023.

[28] L. Lei and Y. Zhou, "Incremental stable/dynamic disentanglement learning for ocean subsurface temperature prediction," *IEEE Trans. Geosci. Remote Sens.*, vol. 63, 2025, Art. no. 4201513.

[29] K. Fukami, K. Fukagata, and K. Taira, "Super-resolution reconstruction of turbulent flows with machine learning," *J. Fluid Mech.*, vol. 870, pp. 106–120, Jul. 2019.

[30] K. Fukami, R. Maulik, N. Ramachandra, K. Fukagata, and K. Taira, "Global field reconstruction from sparse sensors with Voronoi tessellation-assisted deep learning," *Nat. Mach. Intell.*, vol. 3, no. 11, pp. 945–951, 2021.

[31] Z. Zhou, B. Li, X. Yang, and Z. Yang, "A robust super-resolution reconstruction model of turbulent flow data based on deep learning," *Comput. Fluids*, vol. 239, May 2022, Art. no. 105382.

[32] Y. Yasuda and R. Onishi, "Rotationally equivariant super-resolution of velocity fields in two-dimensional flows using convolutional neural networks," *APL Mach. Learn.*, vol. 1, no. 2, Jun. 2023, Art. no. 026107.

[33] J. E. Santos, Z. R. Fox, A. Mohan, D. O'Malley, H. Viswanathan, and N. Lubbers, "Development of the senseiver for efficient field reconstruction from sparse observations," *Nature Mach. Intell.*, vol. 5, no. 11, pp. 1317–1325, Nov. 2023.

[34] S. Chen, L. Zhang, and L. Zhang, "Cross-scope spatial–spectral information aggregation for hyperspectral image super-resolution," *IEEE Trans. Image Process.*, vol. 33, pp. 5878–5891, 2024.

[35] J. Wu, D. Xiao, and M. Luo, "Deep-learning assisted reduced order model for high-dimensional flow prediction from sparse data," *Phys. Fluids*, vol. 35, no. 10, Oct. 2023, Art. no. 103115.

[36] Q. Huang, W. Zhu, F. Ma, Q. Liu, J. Wen, and L. Chen, "Sparse learning model with embedded RIP conditions for turbulence super-resolution reconstruction," *Comput. Methods Appl. Mech. Eng.*, vol. 425, May 2024, Art. no. 116965.

[37] M. Zhang, W. Li, R. Tao, H. Li, and Q. Du, "Information fusion for classification of hyperspectral and LiDAR data using IP-CNN," *IEEE Trans. Geosci. Remote Sens.*, vol. 60, pp. 1–12, 2021.

[38] G. Vivone, "Multispectral and hyperspectral image fusion in remote sensing: A survey," *Inf. Fusion*, vol. 89, pp. 405–417, Jan. 2023.

[39] Z. Wang, Y. Ma, and Y. Zhang, "Review of pixel-level remote sensing image fusion based on deep learning," *Inf. Fusion*, vol. 90, pp. 36–58, Feb. 2023.

[40] G. Wang, N. Zhang, W. Liu, H. Chen, and Y. Xie, "MFST: A multi-level fusion network for remote sensing scene classification," *IEEE Geosci. Remote Sens. Lett.*, vol. 19, pp. 1–5, 2022.

[41] W. Cheng, Y. Feng, L. Song, and X. Wang, "DMF2Net: Dynamic multi-level feature fusion network for heterogeneous remote sensing image change detection," *Knowl.-Based Syst.*, vol. 300, Sep. 2024, Art. no. 112159.

[42] S. Jia et al., "Multiple feature-based superpixel-level decision fusion for hyperspectral and LiDAR data classification," *IEEE Trans. Geosci. Remote Sens.*, vol. 59, no. 2, pp. 1437–1452, Feb. 2020.

[43] L. Goddard and A. Gershunov, "Impact of el niño on weather and climate extremes," in *El Niño Southern Oscillation in a Changing Climate*. Hoboken, NJ, USA: Wiley, 2020, pp. 361–375.

[44] S. Chen, B. Yu, and W. Chen, "An analysis on the physical process of the influence of AO on ENSO," *Climate Dyn.*, vol. 42, nos. 3–4, pp. 973–989, Feb. 2014.

[45] S. Chen et al., "Interdecadal variation in the impact of Arctic sea ice on el Niño–Southern oscillation: The role of atmospheric mean flow," *J. Climate*, vol. 37, no. 21, pp. 5483–5506, Nov. 2024.

[46] N. M. S. D. Center. (2023). *Corta 1.0-WNP-Temperature*. [Online]. Available: http://mds.nmdis.org.cn/

[47] J. Ye, Q. Li, H. Xiong, H. Park, R. Janardan, and V. Kumar, "IDR/QR: An incremental dimension reduction algorithm via QR decomposition," in *Proc. 10th ACM SIGKDD Int. Conf. Knowl. Discovery Data Mining*, Aug. 2004, pp. 364–373.

[48] R. Sun, M. L. Greene, D. M. Le, Z. I. Bell, G. Chowdhary, and W. E. Dixon, "Lyapunov-based real-time and iterative adjustment of deep neural networks," *IEEE Contr. Syst. Lett.*, vol. 6, pp. 193–198, 2021.

[49] S. Hu, W. Zhang, M. Watanabe, F. Jiang, F.-F. Jin, and H.-C. Chen, "Equatorial Western–central Pacific SST responsible for the North Pacific Oscillation–ENSO sequence," *J. Climate*, vol. 37, no. 11, pp. 3191–3204, Jun. 2024.

Lei Lei (Member, IEEE) received the B.E. degree in naval architecture and ocean engineering from the Department of Ship Engineering, Harbin Engineering University, Harbin, China, in 2016, the M.E. degree in mechanical engineering from the Department of Mechanical Science and Engineering, Huazhong University of Science and Engineering, Wuhan, China, in 2019, and the Ph.D. degree from the Department of Systems Engineering, City University of Hong Kong, Hong Kong, in 2024.

He is currently a Postdoctoral Fellow at the Department of Mechanical and Automation Engineering, The Chinese University of Hong Kong, Hong Kong. His research interests include underwater unmanned systems and ocean big data.

Guidong Yang (Graduate Student Member, IEEE) received the B.Eng. degree in mechanical and automation engineering from Shanghai Jiao Tong University (SJTU), Shanghai, China, in 2018, the M.Eng. degree in vehicle engineering from SJTU, in 2021, and the M.Sc. degree in mechanical engineering from the Politecnico di Milano, Milan, Italy, in 2021. He is currently pursuing the Ph.D. degree in mechanical and automation engineering with The Chinese University of Hong Kong, Hong Kong, China.

His research interests include underwater multiview stereo and underwater image enhancement.

Zuoquan Zhao received the M.Sc. degree in control engineering from Zhejiang University, Hangzhou, Zhejiang, China, in 2020. He is currently pursuing the Ph.D. degree in mechanical and automation engineering with The Chinese University of Hong Kong, Hong Kong, SAR, China.

His research interests include unmanned systems, control engineering, and 3-D modeling.

Xi Chen received the B.S. degree in energy and environment systems engineering from Zhejiang University, Hangzhou, China, in 2009, and the M.Phil. and Ph.D. degrees in building environment and energy engineering from The Hong Kong Polytechnic University, Hong Kong, in 2011 and 2017 respectively.

He is now a Research Assistant Professor with Chinese University of Hong Kong, and a Chartered Energy Engineer in Engineering Council (U.K.). He has over ten years experience in sustainable building technologies related to green building, built environment modelling and smart inspection. He has led or managed multiple research projects including Australian Research Council (ARC), Environment and Conservation Fund (ECF), Innovation and Technology Fund (ITF), Research Grants Council (RGC) Hong Kong and industrial consultancy projects with an awarded sum over 10M HKD. He published over 70 papers in peer-reviewed international journals/conferences and coauthored two books in green building, energy efficiency, and renewable application areas with an h-index of 32.

Dr. Chen has been awarded the DECRA (Discovery Early Career Researcher Award) Fellow in the Australian Research Council and Fulbright Scholar in the Lawrence Berkeley National Laboratory. He also services as the editorial board member of *Buildings, Energies, Unmanned Systems* and *Advances in Applied Energy*.

Ben M. Chen (Fellow, IEEE) is a Professor and Chairperson of the Department of Mechanical and Automation Engineering at The Chinese University of Hong Kong (CUHK). Prior to joining CUHK in 2018, he was a Provost's Chair Professor with the Department of Electrical and Computer Engineering, National University of Singapore, where he worked for 28 years. He also served as an Assistant Professor at the State University of New York, Stony Brook, from 1992 to 1993, and worked as a Software Engineer at South China Computer Corporation from 1983 to 1986. He has authored or co-authored hundreds of research articles and ten research monographs in control theory, unmanned systems, and financial market modeling. His current research focuses on unmanned systems and their applications.

Dr Chen is a Fellow of the Academy of Engineering, Singapore. He has served on the editorial boards of several international journals, including Automatica and IEEE TRANSACTIONS ON AUTOMATIC CONTROL. Currently, he is the Editor-in-Chief of *Unmanned Systems* and an Editor of the *International Journal of Robust and Nonlinear Control*.